Physics and Chemistry of Minerals (2022) 49:27
https://doi.org/10.1007/s00269-022-01201-w

ORIGINAL PAPER

Equation of state of elbaite at high pressure up to 21.1 GPa and room temperature

Wei Chen[1,2,3] · Shijie Huang[1,2] · Zhilin Ye[1,2] · Jiamei Song[1,2] · Shanrong Zhang[1,2] · Mengzeng Wu[1,2] · Dawei Fan[1] · Wenge Zhou[1]

Received: 12 March 2022 / Accepted: 23 May 2022 / Published online: 2 July 2022

Abstract

The equation of the state of a natural elbaite sample has been investigated at room temperature and up to 21.1 GPa for the first time using in situ synchrotron X-ray diffraction in this study. No phase transition is observed on elbaite over the experimental pressure range. The pressure–volume data were fitted by the third-order Birch-Murnaghan equation of state (EoS) with the zero-pressure unit-cell volume V_0 = 1540.7 (6) Å^3, the zero-pressure bulk modulus K_{T0} = 114.7 (7) GPa, and its pressure derivative K'_{T0} = 4.2 (1), while obtained V_0 = 1540.1 (4) Å^3 and K_{T0} = 116.4 (4) GPa when fixed K'_{T0} = 4. Furthermore, the axial compressional behavior of elbaite was also fitted with a linearized third-order Birch-Murnaghan EoS, the obtained axial moduli for *a*-axis and *c*-axis are K_{a0} = 201 (4) GPa and K_{c0} = 60 (1) GPa, respectively. The axial compressibilities of *a*-axis and *c*-axis are $\beta_a = 1.66 \times 10^{-3}$ GPa^{-1} and $\beta_c = 5.56 \times 10^{-3}$ GPa^{-1} with an anisotropic ratio of β_a: β_c = 0.30: 1.00, which shows an intense axial compression anisotropy. The potential influencing factors on the bulk moduli and the anisotropic linear compressibilities of tourmalines were further discussed.

Keywords Elbaite · Equation of state · Axial compression anisotropy · Synchrotron X-ray diffraction · High pressure

Introduction

Tourmaline group minerals are the most widespread and abundant borosilicates. They typically occur in a wide variety of granites, granitic pegmatites, sedimentary and metamorphic rocks (Slack 1996; Dutrow and Henry 2011; van Hinsberg et al. 2011; Han et al. 2020; Nabelek 2021; Zhao et al. 2022) and has a wider range of pressure and temperature stability in the Earth's interior (Ota et al. 2008; Dutrow and Henry 2011; van Hinsberg et al. 2011; Henry and Dutrow 2012). The complex crystal chemistry of tourmaline allows its structure to incorporate a large number of elements (Bosi and Lucchesi 2007; Bosi 2018) and tourmaline is stable in the presence of a variety of geological fluids (Meyer et al. 2008; Konzett et al. 2012; Berryman et al. 2016). Furthermore, the compositional zone usually occurred in tourmaline can also maintain stability under relatively high-temperature conditions, mainly due to the very low diffusion rate of major and trace elements and boron isotopes in tourmaline structure (van Hinsberg et al. 2011), thus tourmaline is known as a very valuable indicator mineral of the compositional evolution of their host rocks (e.g., Novák et al. 2004; Maloney et al. 2008; van Hinsberg et al. 2011; Berryman et al. 2017; Kotowski et al. 2020; Qiu et al. 2021). More importantly, as a dominant carrier of boron, tourmaline is the key component of the boron cycle in the deep Earth, especially in subduction zone environments (Nakano and Nakamura 2001; Bebout and Nakamura 2003; Ota et al. 2008; van Hinsberg et al. 2011; Liu and Jiang 2021).

The general formula of tourmaline is $XY_3Z_6T_6O_{18}(BO_3)_3V_3W$, where the site coordinations and main elements at the different sites are as follows: X = Na^+, K^+, Ca^{2+}, □ (= vacancy); Y = Mg^{2+}, Fe^{2+}, Al^{3+}, Li^+, Fe^{3+}, Cr^{3+}, V^{3+}, Mn^{2+}; Z = Al^{3+}, Fe^{3+}, Cr^{3+}, V^{3+}, Mg^{2+}, Fe^{2+}; T = Si^{4+}, Al^{3+}, B^{3+}; B = B^{3+}; V = $(OH)^-$, O^{2-}; W = $(OH)^-$,

✉ Wenge Zhou
zhouwenge@vip.gyig.ac.cn

1 Key Laboratory of High-Temperature and High-Pressure Study of the Earth's Interior, Institute of Geochemistry, Chinese Academy of Sciences, Guiyang 550081, Guizhou, China

2 University of Chinese Academy of Sciences, Beijing 100049, China

3 Guizhou Polytechnic of Construction, Guiyang 551400, Guizhou, China

F^-, O^{2-} (Hawthorne and Henry 1999; Henry et al. 2011). Tourmaline crystallizes in the trigonal system with the space group of *R*3*m* (Fig. 1). Tourmaline is a ring-silicate mineral, with its structure consisting of two basic structural layers. One of the two basic structural layers is six-fold rings of tetrahedral (*T* sites) with a three-fold axis in the *c* direction. On top of six-fold rings of tetrahedral, there are octahedral clusters of the other basic structural layer, arranged of three inner *Y* site and six outer *Z* site octahedral concentrically. The *X* site sits in a nine-coordinated polyhedron above the center of the six-fold ring. B atoms form $[BO_3]^{3-}$ triangles that are linked to the *Y* site and *Z* site octahedra, roughly perpendicular to the *c* axis.

To date, there are about 25 elements that can occur as major components at different sites in the structure of the tourmaline supergroup minerals (e.g., London et al. 2006; Wunder et al. 2015; Setkova et al. 2019; Andreozzi et al. 2020; Pieczka et al. 2020; Vereshchagin et al. 2020; Kutzschbach et al. 2021; Scribner et al. 2021). Among them, the light lithophile cation lithium (Li) can be an important component of tourmaline (van Hinsberg et al. 2011). Elbaite-Li-rich Al tourmaline preferentially forms in chemically evolved granites and related pegmatites, and it is also an important resource of Li (e.g., Keller et al. 1999; Maloney et al. 2008; Bosi et al. 2013; Trumbull et al. 2013; Bronzova et al. 2019; Sunde et al. 2020). Most of the multicolored tourmalines and almost all of the tourmaline gemstones are of the elbaite variety (Pezzotta and Laurs 2011), and elbaite is also one of the most promising pyroelectric materials due to its high pyroelectric coefficient (Ogorodova et al. 2004; Chen et al. 2021).

Insofar, the static compression and equation of state studies of tourmalines (e.g., uvite, dravite, schorl, maruyamite, etc.) have been carried out using the X-ray diffraction (XRD) technique (e.g. Li et al. 2004; Xu et al. 2016; O'Bannon III et al. 2018; Berryman et al. 2019; Likhacheva et al. 2019).

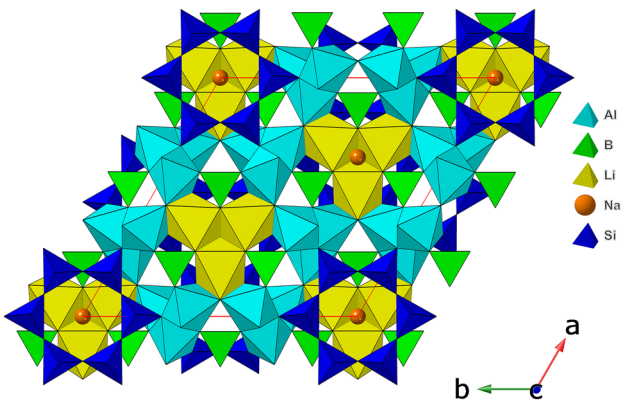

Fig. 1 Crystal structure of elbaite at ambient conditions. The crystal structure data is obtained from Gatta et al. (2012)

Initially, Li et al. (2004) carried out an in situ high-pressure energy-dispersive XRD experiments on a natural tourmaline (schorl) up to 27.8 GPa, and obtained an abnormally high isothermal bulk modulus $K_{T0} = 184$ GPa with fixed its pressure derivative $K'_{T0} = 4$. Hereafter, Xu et al. (2016) studied the thermal equation of state of a natural uvite at simultaneously high pressures and high temperatures up to 18 GPa and 723 K and obtained the thermal equation of state parameters of uvite. And then, O'Bannon III et al. (2018) conducted the synchrotron-based single-crystal XRD measurements of a natural dravite tourmaline at high pressures up to ~ 24 GPa and identified a phase transition of dravite from rhombohedral *R3m* to rhombohedral *R3* occurs at pressures near 15.4 GPa. In addition, Likhacheva et al. (2019) studied the compressibility of a natural maruyamaite (potassium tourmaline) using synchrotron-based single-crystal XRD up to 20 GPa, and discussed the influence of the presence of potassium at the *X*-site on the compressibility and structure behavior of tourmaline at high pressures. Recently, Berryman et al. (2019) collected the high-pressure synchrotron single-crystal XRD patterns of five synthetic Mg–Al tourmalines up to 60 GPa at 300 K, which was used to constrain the equation of state (EoS) of tourmalines with distinct *X*-site occupancies and Mg–Al contents. However, to our knowledge, in addition to the thermal behavior of elbaite has been studied (e.g., Ogorodova et al. 2004; Bosi et al. 2019; Celata et al. 2021), there are no reports in the previous literature about the static compression and equation of state of elbaite (Li-rich Al tourmaline) at high pressures. The high-pressure EoS investigation of elbaite will be helpful to understand the influence of the Li component on the EoS and axial compressibility of tourmalines at high-pressure conditions, and then to gain a comprehensive understanding of the compression property of tourmaline.

In this study, we investigated the EoS of elbaite at high pressures up to 21.1 GPa using diamond anvil cell (DAC) combined with in situ synchrotron radiation XRD. The compression property of elbaite at high-pressure conditions was obtained. In addition, the compressibilities of different tourmalines were compared, and the potential influencing factors were discussed. Moreover, the anisotropic linear compressibilities of tourmalines were also discussed.

Sample and experiment

Sample

The elbaite selected in this study is a natural sample collected from Pakistan with a good crystal morphology, light green, transparent, and columnar. Backscattered electron (BSE) image reveals that the elbaite sample is composition homogeneity and not zoned into different chemical

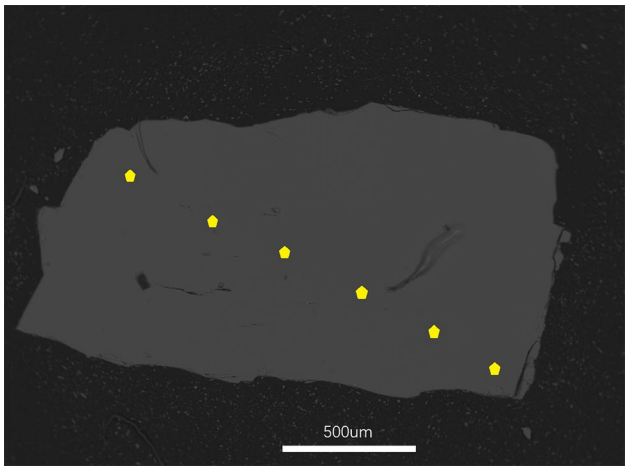

Fig. 2 Backscattered electron image of elbaite. Localities of analyzed spots are also shown as a yellow pentagon

Table 1 Chemical composition of elbaite in this study

Compositions (wt. %)	Elbaite (6)[a]
SiO_2	36.76 (25)
TiO_2	0.01 (1)
Al_2O_3	41.37 (98)
Cr_2O_3	0.01 (1)
MgO	0.01 (1)
FeO[b]	0.91 (76)
MnO	0.15 (8)
NiO	0.01 (1)
ZnO	0.07 (3)
CaO	0.19 (7)
Na_2O	2.03 (14)
K_2O	0.01 (1)
F	0.96 (5)
Total	82.49

Data in the parentheses of compositions represent standard derivations

[a]Number of electron microprobe analyses in parentheses

[b]Total Fe as FeO

domains (Fig. 2). Furthermore, the chemical compositions of the elbaite sample (Table 1) were determined by electron microprobe (EMPA) of thin sections with a JEOL JXA-8230 using a 15 kV accelerating voltage, a 20 nA beam current, and a beam diameter of 5 µm. Element peaks and backgrounds were measured for all elements with counting times of 10 s and 5 s, respectively. The following standards were used: hornblende (SiO_2, TiO_2, MgO, CaO, Na_2O, K_2O, Al_2O_3), gahnite (ZnO), olivine (NiO), pyrope (FeO, MnO, Cr_2O_3) and fluorite (F). Data were reduced online using the ZAF program. Under these conditions, detection limits are approximately 60 ppm for K and Ca, 120 ppm for Fe, Mn, and Ni, 160 ppm for Al, 190 ppm for Cr, Ti, and Mg, 250 ppm for Na, 320 ppm for Si, 360 ppm for Zn, and 480 ppm for F. The chemical formulae of the tourmaline sample was calculated from the results of the EMPA data on a basis of 31 cations using a window program developed by Yavuz et al. (2014). The B_2O_3 content was calculated by assuming 3.00 B apfu, while H_2O was calculated by considering OH + O + F = 4 apfu and V = OH = 3 apfu. The Li (apfu) content was estimated by the formula Li (apfu) = 3-($\sum Y$-site) (Henry and Dutrow 1996). And then the chemical formula was estimated as $(Na_{0.62}Ca_{0.04}\square_{0.34})(Al_{1.90}Li_{0.98}Fe_{0.09}Mn_{0.02})Al_6Si_6O_{18}(BO_3)_3(OH)_3(OH_{0.20},F_{0.48},O_{0.32})$. This chemical composition corresponds to the elbaite species (Henry et al. 2011).

High-pressure and ambient-temperature synchrotron powder XRD experiment

A symmetrical DAC containing a pair of diamond anvils (500 µm culets) mounted on WC seats was employed for the high-pressure and ambient-temperature measurements. Two types of WC seats were used in our synchrotron powder XRD experiment, one is a tapered WC seat (the opening angle is about 60°) which is located at the side of the incident light, and another is a slotted WC seat (the opening angle is about 80°) which is located at the side of the transmitted light. A rhenium (Re) foil with an initial thickness of 250 µm was used as the gasket. The gasket was pre-indented to a thickness of ~ 65 µm, and a hole of 300 µm in diameter was drilled at the center to serve as the sample chamber. The elbaite sample powders mixed with 3 wt. % Au powder which was used as the pressure calibrant for the XRD experiments (Fei et al. 2007) as well as two ruby spheres as pressure indicators for the neon gas-loading (Mao et al. 1986), were loaded into the sample chamber. Neon gas was used as the pressure-transmitting medium by the gas-loading system at the Center for High-Pressure Science and Technology Advanced Research (HPSTAR), China. Because neon gas will crystallize at 4.8 GPa and 300 K and the non-hydrostaticity of neon will appear at 15 GPa and 300 K (Klotz et al. 2009), we evaluated the hydrostatic environment of the sample chamber at each pressure point in our XRD experiment by comparing the measured pressures of two different ruby spheres. We found that the pressure difference between the two different ruby spheres located at different positions of the sample chamber did not exceed 0.3 GPa even at the maximum pressure condition (~ 21 GPa). This is very consistent with the results of previous studies (e.g., Klotz et al. 2009; Berryman et al. 2019), which indicated that neon pressure transmitting medium can provide a good hydrostatic/

quasi-hydrostatic pressure environment in the sample chamber under the maximum experimental pressure of 60 GPa.

The in situ room temperature and high-pressure synchrotron XRD experiments were carried out by angle-dispersive diffraction with diamond-anvil cells at the BL15U1 beamline in the Shanghai Synchrotron Radiation Facility (SSRF) (Zhang et al. 2015). Diffraction images were collected using a MAR-165 charge-coupled device (CCD) detector, placed at a distance of approximately 180 mm to the sample. The detector geometry parameters were calibrated using a CeO_2 diffraction standard. The X-ray beam was monochromatized to a wavelength of 0.6199 Å and focused down to a 2×3 μm^2 area. The typical exposure time for collecting diffraction images of elbaite sample and Au pressure marker was 300 s. XRD patterns of Au were collected at each pressure before and after sample data collection and the average pressure value was taken. The XRD spectra were collected after the experimental pressure was maintained for ~ 60 s. Pressures were calculated from Fei's EoS for Au (Fei et al. 2007) using lattice parameters determined from XRD profiles at each pressure point. The experimental pressure interval in this study was ~ 1–2 GPa, and we finally obtained 17 pressure data points at high pressures up to 21 GPa, which will ensure the accuracy of EoS fitting.

Results

The diffraction patterns were integrated to generate the conventional one-dimensional profiles using the *Fit2D* program (Hammersley et al. 1996). There are about 30 diffraction peaks identified from the XRD patterns and used for the unit-cell parameters and volumes calculation (Fig. 3), which demonstrates the high quality of XRD patterns in this study. And then the diffraction peak positions were fitted by the *Origin 8.5* software. Finally, the unit-cell parameters and volumes were calculated using *UnitCell* software (Holland and Redfern 1997).

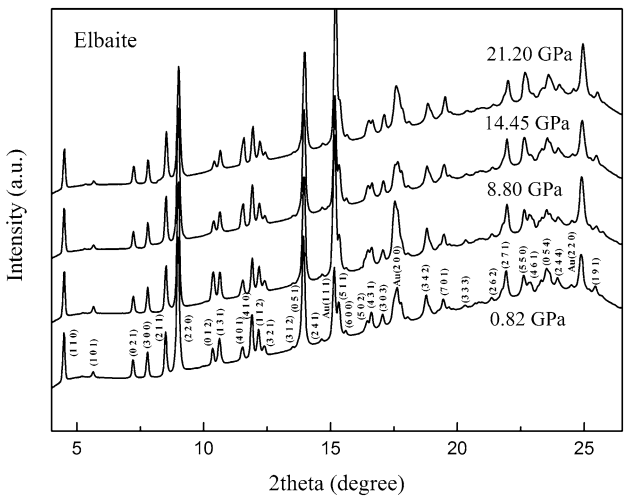

Fig. 3 Representative X-ray diffraction patterns of elbaite in this study up to 21.2 GPa

The XRD patterns of elbaite at various pressures up to 21.1 GPa are shown in Fig. 3. With increasing pressure at room temperature, all the peaks just shifted toward higher 2θ angles. Moreover, the overall diffraction patterns of the elbaite sample did not change within the experimental pressure range (Fig. 3), indicating that there was no structural transition identified in this study. The unit-cell parameters and volumes of elbaite at various pressure conditions are listed in Table 2. Figures 4 and 5 show the volumetric and axial compression of elbaite as a function of the pressure of this study, respectively. The ambient XRD image of elbaite was also collected using the MAR-165 CCD detector in the SSRF and gives the unit-cell parameters and volume of $a_0 = 15.8302$ (12) Å, $c_0 = 7.0988$ (10) Å, and $V_0 = 1540.6$ (2) $Å^3$ for elbaite.

The pressure–volume (*P*–*V*) data (Table 2) were fitted using the third-order Birch-Murnaghan EoS (Birch 1947):

$$P = (3/2)K_{V0}\left[(V_0/V)^{7/3} - (V_0/V)^{5/3}\right] \times\left[1 + 3/4(K'_{V0} - 4)\left[V_0/V\right)^{2/3} - 1\right] \quad (1)$$

where V_0, K_{T0}, and K'_{T0} are the zero-pressure volume, isothermal bulk modulus and its pressure derivative, respectively. Analyses of Eq. (1) by the *EoSFit* program (Angel

Table 2 Unit-cell parameters and volumes of elbaite at ambient temperature and high pressure

P (GPa)	*a* (Å)	*c* (Å)	*V* ($Å^3$)	*a*/*c*
0.00	15.8302 (12)	7.0988 (10)	1540.6 (2)	2.2300
0.82	15.8104 (13)	7.0676 (14)	1529.6 (4)	2.2370
1.95	15.7796 (13)	7.0276 (13)	1515.4 (4)	2.2454
3.24	15.7505 (15)	6.9805 (14)	1499.7 (5)	2.2564
4.60	15.7208 (18)	6.9354 (18)	1484.4 (7)	2.2667
5.80	15.6945 (15)	6.8991 (13)	1471.7 (5)	2.2749
7.15	15.6653 (18)	6.8609 (15)	1458.1 (6)	2.2833
8.80	15.6324 (14)	6.8123 (12)	1441.7 (4)	2.2947
9.80	15.6109 (16)	6.7879 (17)	1432.6 (7)	2.2998
10.35	15.6001 (15)	6.7717 (13)	1427.2 (5)	2.3037
11.10	15.5851 (18)	6.7510 (17)	1420.1 (7)	2.3086
12.05	15.5651 (17)	6.7250 (19)	1411.0 (7)	2.3145
14.45	15.5202 (18)	6.6662 (19)	1390.6 (8)	2.3282
16.20	15.4916 (19)	6.6235 (19)	1376.6 (8)	2.3389
18.55	15.4558 (19)	6.5764 (19)	1360.5 (9)	2.3502
19.90	15.4358 (19)	6.5459 (19)	1350.7 (9)	2.3581
21.10	15.4161 (18)	6.5257 (19)	1343.1 (9)	2.3624

Numbers in parenthesis represent standard deviations

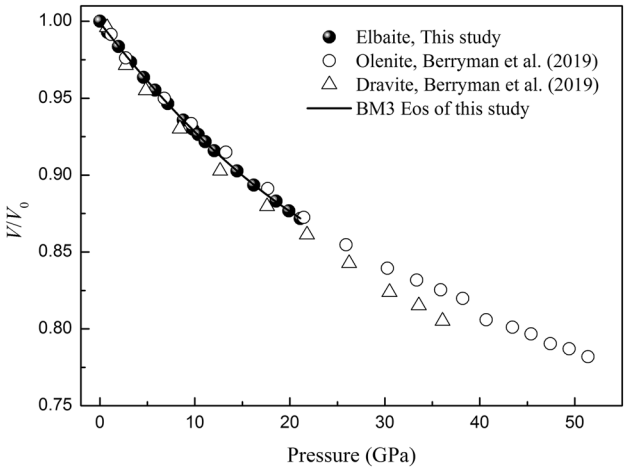

Fig. 4 The volumetric compression of elbaite as a function of pressure, the solid circles represent the data points of elbaite in this study, the hollow circles and and triangles represent the data points of olenite and dravite from Berryman et al. (2019), respectively, and the solid line was obtained by third-order Birch-Murnaghan EoS-fitting of elbaite in this study

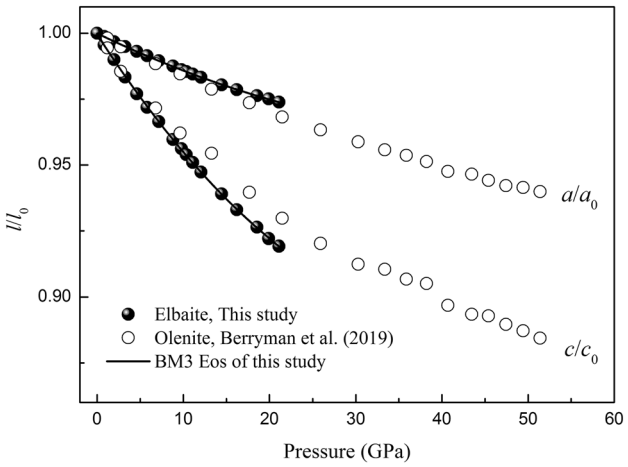

Fig. 5 The axial compression of elbaite as a function of pressure, the solid circles represent the data points of elbaite in this study, the hollow circles represent the data points of olenite from Berryman et al. (2019), and the solid lines were obtained by third-order Birch-Murnaghan EoS-fitting of elbaite in this study

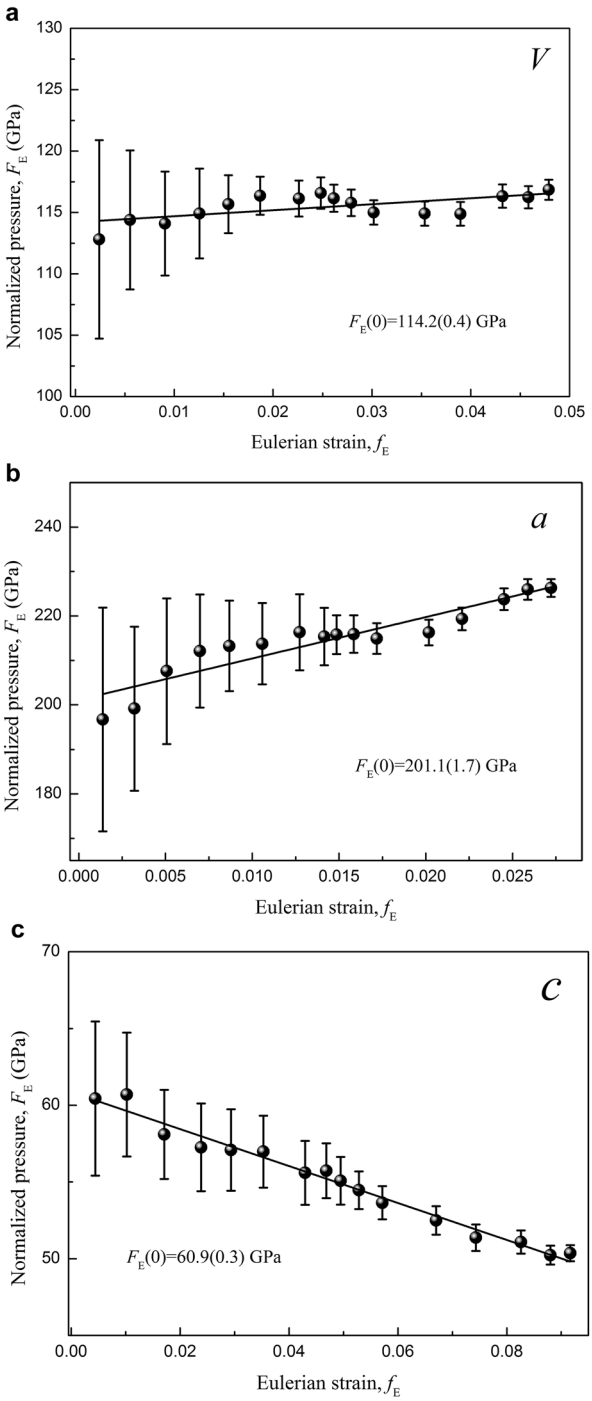

Fig. 6 Volumetric (**a**) and axial (**b** and **c**) Eulerian strain–normalized pressure (F_E–f_E) plots. The solid line is the linear fit of the data

et al. 2014; Gonzalez-Platas et al. 2016) were with all parameters free and the obtained results were as follows: V_0 = 1540.7 (6) Å^3, K_{T0} = 114.7 (7) GPa, and K'_{T0} = 4.2 (1). The refined value of V_0 (1540.7 (6) Å^3) was within 1σ or so compared with the measured V_0 (1540.6 (2) Å^3) by XRD at ambient conditions, indicating excellent accuracy of the refined results (Angel 2000). With the fixed K'_{T0} at 4, the fitting results yielded V_0 = 1540.1 (4) Å^3 and K_{T0} = 116.4 (4) GPa. To evaluate the quality of our third-order Birch-Murnaghan EoS fitting, the relationship between the Eulerian definition of finite strain f_E($f_E = [(V_0/V)^{2/3}-1]/2$) and the "normalized stress" F_E($F_E = P/3f_E(1+2f_E)^{5/2}$) (Birch 1978) is plotted and shown in Fig. 6a. The weighted linear fit of the data points yielded the intercept value of F_E (0) = 114.2 (4) GPa, which is in good agreement with the isothermal bulk modulus obtained by the third-order Birch-Murnaghan

EoS (K_{T0} = 114.7 (7) GPa). Moreover, the function of F_E and f_E had a slightly positive slope, indicating that K'_{T0} is larger than 4 which is consistent with K'_{T0} = 4.2 (1) from the third-order Birch-Murnaghan EoS. Therefore, the third-order Birch-Murnaghan EoS is a reasonable description of the *P*–*V* data in this study.

The axial compressibility (a/a_0 and c/c_0) of elbaite at room temperature is plotted as a function of pressure in Fig. 5. By fitting the unit-cell parameters of elbaite at room temperature using a "linearized" third-order Birch-Murnaghan EoS with the *EosFit* program (Angel et al. 2014; Gonzalez-Platas et al. 2016), the obtained a_0 and c_0 at ambient conditions are 15.8308 (17) Å and 7.0999 (20) Å, respectively. The refined unit-cell parameters are consistent with the results obtained from the XRD measurement at ambient conditions in this study within their uncertainties (Table 2). Simultaneously, the refined linear moduli and their pressure derivatives at ambient conditions are K_{a0} = 201 (4) GPa, K_{c0} = 60 (1) GPa and K'_{a0} = 6.9 (4), K'_{c0} = 2.8 (1), respectively. The slopes obtained from the linear fits of the F_E–f_E plots are fairly positive and negative for the *a* and *c* unit-cell parameters (Fig. 6b and c), respectively. The results are in good agreement with the $K'_{a0} > 4$ and $K'_{c0} < 4$ given by the "linearized" third-order Birch-Murnaghan EoS fits, respectively.

The axial compressibility β_l at ambient conditions has the following form:

$$\beta_l = \frac{1}{(3K_{l0})} \quad (2)$$

In analyses of Eq. (2) with the K_{l0}, we obtained the axial compressibility of *a*- and *c*-axes to be 1.66×10^{-3} GPa^{-1} and 5.56×10^{-3} GPa^{-1}, respectively. It can be known that elbaite has a strong axial compressive anisotropy. The compressibility of elbaite along the *c*-axis is 3.35 times larger than that along *a*-axis (Fig. 5).

Discussion

Although no previous studies reported the *P*–*V* equation of state of elbaite, the *P*–*V* equation of states of other tourmalines (e.g., uvite, dravite, maruyamaite etc.) have been investigated by some previous synchrotron-based XRD experiments. Table 3 summarizes a comparison of the K_{T0} and K'_{T0} of elbaite obtained in this study with the results of other tourmalines given by previous studies. In general, the obtained K_{T0} and K'_{T0} values (114.7 GPa and 4.2, respectively) of elbaite are landing somewhere in between Mg–Al tourmalines (dravite, K-dravite, oxy-uvite, and magnesio-foitite, etc.) and Al-tourmaline (olenite) (Table 3). This is not surprising because the ambient unit-cell volume of elbaite (1540.7 Å^3) is also falling in between Mg–Al tourmalines (1556–1573 Å^3) and Al-tourmaline (1490 Å^3) (Table 3).

From Table 3, we can find that most K'_{T0} values of tourmalines are within the range of 3.5–5.0, except a natural uvite-dominated tourmaline from Xu et al. (2016), who reported a larger K'_{T0} value (12.4). The exact reason for the larger K'_{T0} value reported by Xu et al. (2016) remains unclear. However, Hofmeister (1993) showed that the K'_{T0}

Table 3 The compressibility of elbaite at high pressures and compared with other tourmalines

Sample	K_{T0} (GPa)	K'_{T0}	V_0 (Å^3)	References
Elbaite	114.7 (7)	4.2 (1)	1540.7 (6)	This study
	116.4 (4)	4.0 (fixed)	1540.1 (4)	
Dravite	97 (6)	5.0 (5)	1556 (4)	Berryman et al. (2019)
	110 (2)	4.0 (fixed)	1551 (3)	
K-dravite	109 (4)	4.3 (2)	1567 (3)	
	115 (1)	4.0 (fixed)	1564 (2)	
Oxy-uvite	110 (2)	4.1 (1)	1573 (2)	
	112.5 (6)	4.0 (fixed)	1571 (1)	
Magnesio-foitite	116 (2)	3.5 (1)	1560 (2)	
	105.8 (9)	4.0 (fixed)	1568 (2)	
Olenite	116 (6)	4.7 (4)	1490 (4)	
	128 (2)	4.0 (fixed)	1485 (3)	
Maruyamaite	112 (3)	4.5 (4)	1588 (1)	Likhacheva et al. (2019)
	115.6 (9)	4.0 (fixed)	1587.2 (7)	
Dravite	110 (3)	4.6 (8)	1578.2 (2)	O'Bannon et al. (2018)
	112 (1)	4.0 (fixed)	1578.2 (2)	
Uvite	97 (1)	12.4 (4)	1537 (1)	Xu et al. (2016)
	120 (2)	4.0 (fixed)	1537 (1)	
Schorl	184 (4)	4.0 (fixed)	–	Li et al. (2004)

value of solid materials exceeding 8.0 will lead to physically unrealistic potentials and hence are not appropriate for the EoS. Thus, the reported K'_{T0} value of Xu et al. (2016) is debatable. In addition, the obtained K'_{T0} (3.5) of magnesio-foitite by Berryman et al. (2019) is slightly smaller than the results of other tourmalines. They indicated that the presence of a fully vacant *X* site in magnesio-foitite is a possible cause for the smaller K'_{T0} compared with alkai and Ca tourmalines. But for other tourmalines, their K'_{T0} values are very consistent within their uncertainties (Table 3). Thus, we conclude that the compositional effect on K'_{T0} in tourmaline is very limited, except for the fully vacant at *X* site of tourmaline.

In addition, a detailed analysis of the results of this study and previous studies also shows that there is still some debate about K_{T0} values of tourmalines (97–184 GPa) (Table 3). We infer that there are three possible reasons for the difference K_{T0} of tourmaline reported by this study and previous studies, which are the different pressure mediums, K'_{T0} values, and mineral compositions.

First, Li et al. (2004) measured the compressibility of a natural tourmaline (schorl) at high pressures up to 27.8 GPa using the energy-dispersive XRD method with methanol: ethanol: water = 16:3:1 pressure medium and obtained an abnormally large result of $K_{T0} = 184$ (4) GPa (with fixed $K'_{T0} = 4$). The experimental maximum pressure (~ 27.8 GPa) of Li et al. (2004) seriously exceeds the hydrostatic pressure condition (~ 10 GPa) of the methanol: ethanol: water = 16:3:1 pressure medium (Angel et al. 2007; Klotz et al. 2009), thus the obtained $K_{T0} = 184$ (4) GPa by Li et al. (2004) should be inaccurate.

In addition, in static compression studies, there is a trade-off between the fitted K_{T0} and K'_{T0}, which have a negative correlation. Such as, the obtained K_{T0} values of Xu et al. (2016) and Berryman et al. (2019) are 97 (1) GPa and 97 (6) GPa for uvite and dravite, respectively, which are obviously smaller than those of other tourmalines (Table 3), mainly due to the distinct larger K'_{T0} values ($K'_{T0} = 12.4$ and $K'_{T0} = 5.0$ for uvite and dravite, respectively). However, when fixed $K'_{T0} = 4$, Xu et al. (2016) and Berryman et al. (2019) obtained $K_{T0} = 120$ (2) GPa and $K_{T0} = 110$ (2) GPa of uvite and dravite, respectively, which are relatively close to the results of previous studies for other tourmalines (Table 3).

Furthermore, the mineral composition of tourmaline may also affect the K_{T0} when the K'_{T0} is fixed to 4. For example, the obtained $K_{T0} = 116.4$ (4) GPa for elbaite in this study and $K_{T0} = 110$ (2) GPa for dravite from Berryman et al. (2019) are ~ 9.1% and ~ 14.1% lower than the reported $K_{T0} = 128$ (2) GPa by Berryman et al. (2019) for olenite (Fig. 4), respectively. If we compare the effective ionic radii of cations in the *Y* site of tourmaline, we can find that the effective ionic radii of Li^{1+}(VI) (0.751 Å) and Mg^{2+}(VI) (0.723 Å) at *Y* site are ~ 37.3% and ~ 32.2% larger than Al^{3+}(VI) (0.547 Å) (Bosi and Lucchesi 2007). These cause that the mean bond lengths of Li^{1+}-O (2.211 Å) and Mg^{2+}-O (2.0991 Å) at *Y* site in tourmaline are ~ 16.1% and ~ 10.2% larger than the mean bond length of Al^{3+}-O (1.9043) at *Y* site in tourmaline (Bačík and Fridrichová 2021). The bond strengths of Li^{1+}-O and Mg^{2+}-O at *Y* sites in elbaite and dravite, respectively, are weaker than that of the Al^{3+}-O at *Y* site in olenite due to the larger bond length; accordingly, elbaite and dravite have larger compressibility and smaller isothermal bulk modulus. In addition, the reported $K_{T0} = 105.8$ (9) GPa for magnesio-foitite from Berryman et al. (2019) is ~ 6.0% lower than that of oxy-uvite ($K_{T0} = 112.5$ (6) GPa), which is believed to be correlated with the presence of a nearly completely vacant *X* site in magnesio-foitite (Berryman et al. 2019). Thus, based on the above discussion, we infer that the bond strengths of the corresponding bonds at *Y* site and significant *X* site vacancies likely have an important effect on the compressibility of the tourmaline.

Finally, if the influence of external factors such as the different pressure medium is excluded, we believe that the reasonable ranges of the K_{T0} and K'_{T0} of tourmalines should be 106–128 GPa and 3.5–5.0, respectively.

The axial compressibility of the elbaite sample in this study shows the compressive behavior of the *c*-axis direction is comparably softer than the *a*-axis direction with a description of $\beta_a = 1.66 \times 10^{-3}$ GPa^{-1} and $\beta_c = 5.56 \times 10^{-3}$ GPa^{-1}. Our results confirm again that tourmaline is highly anisotropic elasticity, where the *c*-axis is about 3.35 times more compressible than the *a*-axis under ambient conditions. Similar anisotropic compression behaviors have been reported for natural dravite, uvite, maruyamaite, and synthetic Mg–Al tourmalines (Xu et al. 2016; O'Bannon III et al. 2018; Berryman et al. 2019; Likhacheva et al. 2019). We infer there are two possible reasons for the compression anisotropy with $\beta_c > \beta_a$ of tourmaline species. One possible reason is the incorporation of relatively larger molecular water in the *c*-parallel structural channels in tourmaline (Bosi 2018), which results in the more compressible *c*-axis in the structure of tourmaline. Another possible reason is that the gaps between [Si6O18] rings in the *a*-axis direction of tourmaline are relatively small and thus it is difficult to compress, while the [Si6O18] six-fold rings and cationic octahedral layers are arranged in the *c*-axis direction of tourmaline (Bosi and Lucchesi 2007; Bosi 2018), which can be refilled with larger cations with large voids, so it is easy to be compressed in the *c*-axis direction. Finally, the anisotropic compression behavior of tourmaline is similar to other cyclosilicates (e.g., beryl and cordierite) (e.g., Fan et al. 2015; Finkelstein et al. 2015) and is interpreted to reflect the relative incompressibility of the ring structure parallel to *a*-axis.

Furthermore, the axial compression of the *a*-axis and *c*-axis for elbaite in this study is slightly smaller and much larger than those of olenite in the Berryman et al. (2019) (Fig. 5), respectively, which indicates that the axial

compression anisotropy of elbaite in this study is larger than that of olenite in the Berryman et al. (2019). Considering the bulk modulus of elbaite is lower than that of olenite, we thus infer that compared with olenite, the Li component at *Y* site increases the compressibility of elbaite. And the possible reason for the higher compressibility of elbaite is mainly the reduced stiffness in the *c*-axis of elbaite. This is very consistent with the conclusion of Berryman et al. (2019), who pointed out that the lower compressibility of olenite is primarily accounted for by its reduced axial compressibility along the *c*-axis.

Conclusion

The *P*–*V* relationship of elbaite was carried out using the synchrotron-based single-crystal XRD method up to 21.1 GPa in this study. There was no phase transition in the maximum pressure conditions in this study. Fitted the *P*–*V* data by third-order Birch-Murnaghan EoS, obtained $V_0 = 1540.7$ (6) Å^3, $K_{T0} = 114.7$ (7) GPa, and $K'_{T0} = 4.2$ (1) for elbaite. Simultaneously, we also obtained the axial compressibility for elbaite along *a*-axis ($\beta_a = 1.66 \times 10^{-3}$ GPa^{-1}) and *c*-axis ($\beta_c = 5.56 \times 10^{-3}$ GPa^{-1}). In addition, we further discussed the possible reasons for the different K_{T0} and K'_{T0} among tourmalines, and find that compositional effect on K'_{T0} in tourmaline is limited, except for the fully vacant at *X* site of tourmaline, and the different pressure mediums, K'_{T0} values and mineral compositions may all affect the reported bulk moduli of tourmalines. Finally, we also discussed the potential influencing factors on the anisotropic linear compressibilities of tourmalines, and infer that the possible reason for the higher compressibility of elbaite compared with olenite is mainly the reduced stiffness in the *c*-axis of elbaite.

Acknowledgements This project was supported by the National Natural Science Foundation of China (U2032118 and 42172048), the Youth Innovation Promotion Association CAS (Dawei Fan, 2018434), the Chinese Academy of Sciences "Light of West China" Program (2019), the Science and Technology Foundation of Guizhou Province (QKHJC-ZK[2021]ZD042), and the Guizhou Provincial 2020 Science and Technology Subsidies (No. GZ2020SIG). The high-pressure XRD experiments were conducted at the BL15U1 of the Shanghai Synchrotron Radiation Facility (SSRF). We acknowledge H.Y. Su for the neon gas loading assistance.

References

Andreozzi GB, Bosi F, Celata B, Capizzi LS, Stagno V, Beckett-Brown CE (2020) Crystal-chemical behavior of Fe^{2+} in tourmaline dictated by structural stability: insights from a schorl with formula $Na^{Y}(Fe^{2+}{}_2Al)^{Z}(Al_5Fe^{2+})(Si_6O_{18})(BO_3)_3(OH)_3(OH, F)$ from Seagull batholith (Yukon Territory, Canada). Phys Chem Miner 47:25. https://doi.org/10.1007/s00269-020-01094-7

Angel RJ (2000) Equations of state. Rev Miner Geochem 41:35–59. https://doi.org/10.2138/rmg.2000.41.2

Angel RJ, Bujak M, Zhao J, Gatta GD, Jacobsen SD (2007) Effective hydrostatic limits of pressure media for high-pressure crystallographic studies. J Appl Cryst 40:26–32. https://doi.org/10.1107/S0021889806045523

Angel RJ, Gonzalez-Platas J, Alvaro M (2014) EosFit-7c and a Fortran module (library) for equation of state calculations. Z Kristallogr 229:405–419. https://doi.org/10.1515/zkri-2013-1711

Bačík P, Fridrichová J (2021) Cation partitioning among crystallographic sites based on bond-length constraints in tourmaline-supergroup minerals. Am Miner 106:851–861. https://doi.org/10.2138/am-2021-7804

Bebout G, Nakamura E (2003) Record in metamorphic tourmalines of subduction-zone devolatilization and boron cycling cycling record in metamorphic tourmalines of subduction-zone devolatilization and boron cycling. Geology 31:407–410. https://doi.org/10.1130/0091-7613(2003)031%3c0407:RIMTOS%3e2.0.CO;2

Berryman EJ, Wunder B, Rhede D, Schettler G, Franz G, Heinrich W (2016) *P*-*T*–*X* controls on Ca and Na distribution between Mg–Al tourmaline and fluid. Contrib Miner Pet 171:31. https://doi.org/10.1007/s00410-016-1246-8

Berryman EJ, Kutzschbach M, Trumbull RB, Meixner A, van Hinsberg V, Kasemann SA, Franz G (2017) Tourmaline as a petrogenetic indicator in the Pfitsch Formation, Western Tauern Window, Eastern Alps. Lithos 284–285:138–155. https://doi.org/10.1016/j.lithos.2017.04.008

Berryman EJ, Zhang DZ, Wunder B, Duffy TS (2019) Compressibility of synthetic Mg-Al tourmaline to 60 GPa. Am Mineral 104:1005–1015. https://doi.org/10.2138/am-2019-6967

Birch F (1947) Finite elastic strain of cubic crystals. Phys Rev 71:809–924. https://doi.org/10.1103/PhysRev.71.809

Birch F (1978) Finite strain isotherm and velocities for single-crystal and polycrystalline NaCl at high pressures and 300°K. J Geophys Res-Sol Ea 83:1257–1268. https://doi.org/10.1029/JB083iB03p01257

Bosi F (2018) Tourmaline crystal chemistry. Am Miner 103:298–306. https://doi.org/10.2138/am-2018-6289

Bosi F, Lucchesi S (2007) Crystal chemical relationships in the tourmaline group: structural constraints on chemical variability. Am Miner 92:1054–1063. https://doi.org/10.2138/am.2007.2370

Bosi F, Andreozzi GB, Skogby H, Lussier AJ, Abdu Y, Hawthorne FC (2013) Fluor-elbaite, $Na(Li_{1.5}Al_{1.5})Al_6(Si_6O_{18})(BO_3)_3(OH)_3F$, a new mineral species of the tourmaline supergroup. Am Miner 98:297–303. https://doi.org/10.2138/am.2013.4285

Bosi F, Skogby H, Hålenius U (2019) Thermally induced cation redistribution in fluor-elbaite and Fe-bearing tourmalines. Phys Chem Miner 46:371–383. https://doi.org/10.1007/s00269-018-1009-3

Bronzova Y, Babushkina M, Frank-Kamenetskaya O, Vereshchagin O, Rozhdestvenskaya I, Zolotarev A (2019) Short-range order in Li–Al tourmalines: IR spectroscopy, X-ray single crystal diffraction analysis and a bond valence theory approach. Phys Chem Miner 46:815–825. https://doi.org/10.1007/s00269-019-01042-0

Celata B, Ballirano P, Andreozzi GB, Bosi F (2021) In situ high-temperature behaviour of fluor-elbaite: breakdown conditions and products. Phys Chem Miner 48:24. https://doi.org/10.1007/s00269-021-01147-5

Chen F, Guo JS, Meng DZ, Wu YT, Sun RJ, Zhao CC (2021) Strong pyro-electro-chemical coupling of elbaite/h_2o_2 system for pyrocatalysis dye wastewater. Catalysts 11(11):1370. https://doi.org/10.3390/catal11111370

Dutrow BL, Henry DJ (2011) Tourmaline: a geologic DVD. Elements 7:301–306. https://doi.org/10.2113/gselements.7.5.301

Fan DW, Xu JG, Kuang YQ, Li XD, Li YC, Xie HS (2015) Compressibility and equation of state of beryl ($Be_3Al_2Si_6O_{18}$) by using a diamond anvil cell and in situ synchrotron X-ray diffraction. Phys Chem Miner 42:529–539. https://doi.org/10.1007/s00269-015-0741-1

Fei YW, Ricolleau A, Frank M, Mibe K, Shen GY, Prakapenka V (2007) Toward an internally consistent pressure scale. PNAS 104(22):182–9186. https://doi.org/10.1073/pnas.0609013104

Finkelstein GJ, Dera PK, Duffy TS (2015) High-pressure phases of cordierite from single-crystal X-ray diffraction to 15 GPa. Am Miner 100(8–9):1821–1833. https://doi.org/10.2138/am-2015-5073

Gatta GD, Danisi RM, Adamo I, Meven M, Diella V (2012) A single-crystal neutron and X-ray diffraction study of elbaite. Phys Chem Miner 39:577–588. https://doi.org/10.1007/s00269-012-0513-0

Gonzalez-Platas J, Alvaro M, Nestola F, Angel R (2016) EosFit7-GUI: a new graphical user interface for equation of state calculations, analyses and teaching. J Appl Cryst 49:1377–1382. https://doi.org/10.1107/S1600576716008050

Hammersley AP, Svensson SO, Hanfland M, Fitch AN, Hausermann D (1996) Two-dimensional detector software: From real detector to idealised image or two-theta scan. High Pressure Res 14:235–248. https://doi.org/10.1080/08957959608201408

Han JS, Hollings P, Jourdan F, Zeng YC, Chen HY (2020) Inherited Eocene magmatic tourmaline captured by the Miocene Himalayan leucogranites. Am Miner 105:1436–1440. https://doi.org/10.2138/am-2020-7608

Hawthorne FC, Henry DJ (1999) Classification of the minerals of the tourmaline group. Eur J Miner 11(2):201–215

Henry DJ, Dutrow BL (1996) Metamorphic tourmaline and its petrologic applications. Rev Miner Geochem 33:503–557

Henry DJ, Dutrow BL (2012) Tourmaline at diagenetic to low-grade metamorphic conditions: its petrologic applicability. Lithos 154:16–32. https://doi.org/10.1016/j.lithos.2012.08.013

Henry DJ, Novák M, Hawthorne FC, Ertl A, Dutrow BL, Uher P, Pezzotta F (2011) Nomenclature of the tourmaline-supergroup minerals. Am Miner 96:895–913. https://doi.org/10.2138/am.2011.3636

Hofmeister AM (1993) Interatomic potentials calculated from equations of state: Limitation of finite strain to moderate K'. Geophys Res Lett 20(7):635–638. https://doi.org/10.1029/93GL00388

Holland TJB, Redfern SAT (1997) Unit cell refinement from powder diffraction data: the use of regression diagnostics. Miner Mag 61:5–77

Keller P, Roda-Robles E, Pesquera-Pérez A, Fontan F (1999) Chemistry, paragenesis and significance of tourmaline in pegmatites of the Southern Tin Belt, central Namibia. Chem Geol 158:203–225. https://doi.org/10.1016/S0009-2541(99)00045-5

Klotz S, Chervin JC, Munsch P, Marchand GL (2009) Hydrostatic limits of 11 pressure transmitting media. J Phys D 42:075413. https://doi.org/10.1107/S0021889806045523

Konzett J, Krenn K, Hauzenberger CH, Whitehouse M, Hoinkes G (2012) High-pressure tourmaline formation and fluid activity in Fe-Ti-rich eclogites from the Kreuzeck Mountains, eastern Alps. Austria J Pet 53(1):9–125. https://doi.org/10.1093/petrology/egr057

Kotowski J, Nejbert K, Olszewska-Nejbert D (2020) Tourmalines as a tool in provenance studies of terrigenous material in extra-Carpathian Albian (uppermost lower cretaceous) sands of Miechów Synclinorium. South Poland Miner 10:0917. https://doi.org/10.3390/min10100917

Kutzschbach M, Wunder B, Wannhoff I, Wilke FDH, Couffignal F, Rocholl A (2021) Raman spectroscopic quantification of tetrahedral boron in synthetic aluminum-rich tourmaline. Am Miner 106:872–882. https://doi.org/10.2138/am-2021-7758

Li HJ, Qin S, Zhu XP, Liu J, Li XD, Wu X, Wu ZY (2004) In situ high-pressure X-ray diffraction of natural tourmaline. Nucl Tech 27(12):19–922. https://doi.org/10.3321/j.issn:0253-3219.2004.12.009 (**in Chinese**)

Likhacheva AY, Rashchenko SV, Musiyachenko KA, Korsakov AV, Collings IE, Hanfland M (2019) Compressibility and structure behavior of maruyamaite (K-tourmaline) from the Kokchetav massif at high pressure up to 20 GPa. Miner Pet 113:613–623. https://doi.org/10.1007/s00710-019-00672-0

Liu T, Jiang SY (2021) Multiple generations of tourmaline from Yushishanxi leucogranite in South Qilian of western China record a complex formation history from B-rich melt to hydrothermal fluid. Am Miner 106:994–1008. https://doi.org/10.2138/am-2021-7473

London D, Ertl A, Hughes JM, Morgan GBVI, Fritz EA, Harms BS (2006) Synthetic Ag-rich tourmaline: structure and chemistry. Am Miner 91:680–684. https://doi.org/10.2138/am.2006.1959

Maloney JS, Nabelek PI, Sirbescu MC, Halama R (2008) Lithium and its isotopes in tourmaline as indicators of the crystallization process in the San Diego County pegmatites, California, USA. Eur J Miner 20:905–916. https://doi.org/10.1127/0935-1221/2008/0020-1823

Mao HK, Xu J, Bell PM (1986) Calibration of the ruby pressure gauge to 800 kbar under quasi-hydrostatic conditions. J Geophys Res 91(B5):4673–4676. https://doi.org/10.1029/JB091iB05p04673

Meyer C, Wunder B, Meixner A, Romer RL, Heinrich W (2008) Boron-isotope fractionation between tourmaline and fluid: an experimental re-investigation. Contrib Miner Pet 156:259–267. https://doi.org/10.1007/s00410-008-0285-1

Nabelek PI (2021) Formation of metasomatic tourmalinites in reduced schists during the Black Hills Orogeny, South Dakota. Am Miner 106:282–289. https://doi.org/10.2138/am-2020-7405

Nakano T, Nakamura E (2001) Boron isotope geochemistry of metasedimentary rocks and tourmalines in a subduction zone metamorphic suite. Phys Earth Planet 127:233–252. https://doi.org/10.1016/S0031-9201(01)00230-8

Novák M, Povondra P, Selway JB (2004) Schorl-oxy-schorl to dravite-oxy-dravite tourmaline from granitic pegmatites; examples from the Moldanubicum, Czech Republic. Eur J Miner 16:323–333. https://doi.org/10.1127/0935-1221/2004/0016-0323

O'Bannon E III, Beavers CM, Kunz M, Williams Q (2018) High-pressure study of dravite tourmaline: insights into the accommodating nature of the tourmaline structure. Am Miner 103:1622–1633. https://doi.org/10.2138/am-2018-6486

Ogorodova LP, Melchakova LV, Kiseleva IA, Peretyazhko IS (2004) Thermodynamics of natural tourmaline-elbaite. Thermochim Acta 419:211–214. https://doi.org/10.1016/j.tca.2003.12.019

Ota T, Kobayashi K, Katsura T, Nakamura E (2008) Tourmaline breakdown in a pelitic system: implications for boron cycling through subduction zones. Contrib Miner Pet 155:19–32. https://doi.org/10.1007/s00410-007-0228-2

Pezzotta F, Laurs BM (2011) Tourmaline: the kaleidoscopic gemstone. Elements 7:333–338. https://doi.org/10.2113/gselements.7.5.333

Pieczka A, Ertl A, Gołębiowska B, Jeleń P, Kotowski J, Nejbert K, Stachowicz M, Giester G (2020) Crystal structure and Raman spectroscopic studies of OH stretching vibrations in Zn-rich fluor-elbaite. Am Miner 105:1622–1630. https://doi.org/10.2138/am-2020-7360

Qiu KF, Yu HC, Hetherington C, Huang YQ, Yang T, Deng J (2021) Tourmaline composition and boron isotope signature as a tracer of magmatic-hydrothermal processes. Am Miner 106:1033–1044. https://doi.org/10.2138/am-2021-7495

Scribner ED, Cempírek J, Groat LA, Evans RJ, Biagioni C, Bosi F, Dini A, Hålenius U, Orlandi P, Pasero M (2021) Magnesio-lucchesiite, $CaMg_3Al_6(Si_6O_{18})(BO_3)_3(OH)_3O$, a new species of the tourmaline supergroup. Am Miner 106:862–871. https://doi.org/10.2138/am-2021-7496

Setkova TV, Balitsky VS, Shapovalov YB (2019) Experimental study of the stability and synthesis of the tourmaline supergroup

minerals. Geochem Int 57:082–1094. https://doi.org/10.1134/S0016702919100094

Slack JF (1996) Tourmaline associations with hydrothermal ore deposits. In: Grew ES, Anovitz LM (eds) Mineralogy, petrology and geochemistry, 33rd edn. De Gruyter, Boron, pp 559–644

Sunde Ø, Friis H, Andersen T, Trumbull RB, Wiedenbeck M, Lyckberg P, Agostini S, Casey WH, Yu P (2020) Boron isotope composition of coexisting tourmaline and hambergite in alkaline and granitic pegmatites. Lithos 352–353:105293. https://doi.org/10.1016/j.lithos.2019.105293

Trumbull RB, Beurlen H, Wiedenbeck M, Soares DR (2013) The diversity of B-isotope variations in tourmaline from rare-element pegmatites in the Borborema Province of Brazil. Chem Geol 352:47–62. https://doi.org/10.1016/j.chemgeo.2013.05.021

van Hinsberg VJ, Henry DJ, Marschall HR (2011) Tourmaline: an ideal indicator of its host environment. Can Miner 49:1–16. https://doi.org/10.3749/canmin.49.1.1

Vereshchagin OS, Wunder B, Britvin SN, Frank-Kamenetskaya OV, Wilke FDH, Vlasenko NS, Shilovskikh VV (2020) Synthesis and crystal structure of Pb-dominant tourmaline. Am Miner 105:1589–1592. https://doi.org/10.2138/am-2020-7457

Wunder B, Berryman E, Plessen B, Rhede D, Koch-Müller M, Heinrich W (2015) Synthetic and natural ammonium-bearing tourmaline. Am Miner 100:250–256. https://doi.org/10.2138/am-2015-5055

Xu JG, Kuang YQ, Zhang B, Liu YG, Fan DW, Li XD, Xie HS (2016) Thermal equation of state of natural tourmaline at high pressure and temperature. Phys Chem Miner 43:315–326. https://doi.org/10.1007/s00269-015-0796-z

Yavuz F, Karakaya N, Yildirim DK, Karakaya MC, Kumral M (2014) A Windows program for calculation and classification of tourmaline-supergroup (IMA-2011). Comput Geosci 63:70–87. https://doi.org/10.1016/j.cageo.2013.10.012

Zhang LL, Yan S, Jiang S, Yang K, Wang H, He SM, Liang DX, Zhang L, He Y, Lan XY, Mao CW, Wang J, Jiang H, Zheng Y, Dong ZH, Zeng LY, Li AG (2015) Hard X-ray micro-focusing beamline at SSRF. Nucl Sci Tech 26:60101. https://doi.org/10.13538/j.1001-8042/nst.26.060101

Zhao Z, Yang XY, Lu YY, Zhang ZZ, Chen SS, Sun C, Hou Q, Wang Y, Li S (2022) Geochemistry and boron isotope compositions of tourmalines from the granite-greisen-quartz vein system in Dayishan pluton, Southern China: implications for potential mineralization. Am Miner 107:495–508. https://doi.org/10.2138/am-2021-7591